Well-balanced high-order solver for blood flow in networks of vessels with variable properties

Lucas O. Müller[*,†] and Eleuterio F. Toro

Laboratory of Applied Mathematics, Department of Civil, Environmental and Mechanical Engineering, University of Trento, Via Mesiano 77, I-38100 Trento, Italy

ABSTRACT

We present a well-balanced, high-order non-linear numerical scheme for solving a hyperbolic system that models one-dimensional flow in blood vessels with variable mechanical and geometrical properties along their length. Using a suitable set of test problems with exact solution, we rigorously assess the performance of the scheme. In particular, we assess the well-balanced property and the effective order of accuracy through an empirical convergence rate study. Schemes of up to fifth order of accuracy in both space and time are implemented and assessed. The numerical methodology is then extended to realistic networks of elastic vessels and is validated against published state-of-the-art numerical solutions and experimental measurements. It is envisaged that the present scheme will constitute the building block for a closed, global model for the human circulation system involving arteries, veins, capillaries and cerebrospinal fluid. Copyright © 2013 John Wiley & Sons, Ltd.

1. INTRODUCTION

One-dimensional blood flow models are nowadays widely applied in the active field of cardiovascular mathematics. They can be used, for example, as stand-alone tools [1–4] or combined with multidimensional fluid–structure interaction models [5] in a multiscale framework. One-dimensional models can also be used to solve inverse problems to compute patient-specific cardiovascular network characteristics, as performed recently in [6]. It is reasonable to assume that for the foreseeable future, one-dimensional models will play a crucial role in any attempt to construct closed, global models for the human circulation system. It is therefore of paramount importance to construct such models on solid physical, mathematical and numerical basis.

In the modelling of many physiological situations, it may be relevant to consider the variation of mechanical and geometrical properties of blood vessels along their length, such as tapering of arteries and situations arising from endovascular repair [7], for example. The presence of such variations gives rise to *geometric-type* source terms and prevents expressing the governing equations in conservation-law form, in terms of conserved variables. The mathematical analysis and the numerical approximation of such systems require special care. If *geometric-type* source terms are treated in a conventional manner, spurious oscillations may be generated in the numerical solution; in the presence of large gradients or discontinuities, codes may simply crash. Moreover, the resulting schemes will be unable to correctly compute special but important cases, such as steady or stationary solutions [8, 9].

---

*Correspondence to: Lucas O. Müller, Laboratory of Applied Mathematics, Department of Civil, Environmental and Mechanical Engineering, University of Trento, Via Mesiano 77, I-38100, Trento, Italy.
†E-mail: lucas.mueller@gmail.com

The subject of one-dimensional models for blood flow in the presence of discontinuous material properties has been addressed in the past. Examples include Čanič [7] and the more recent work of Toro and Siviglia [10]. In [10], the authors put forward a simple mathematical model for one-dimensional blood flow in vessels with variable, even discontinuous, mechanical properties. This model has very recently been extended [11] to include other relevant parameters, such as reference cross-sectional area and external pressure. In both [10] and [11], Toro and Siviglia propose a new mathematical formulation of the problem, carry out a thorough analysis of the equations and provide the exact solution of the resulting Riemann problem (RP) in the case of discontinuous variation of mechanical and geometrical properties. In both of these works, the authors draw attention to the challenging problem of designing suitable numerical methods to solve the hyperbolic equations accurately.

The refined numerical treatment of source terms in hyperbolic balance laws was first addressed by Roe [12]. In analogy to the choice of numerical fluxes, Roe proposed the use of *upwinding* as a way of devising better numerical schemes for source terms. Effective schemes along these lines were later proposed by various authors, see [13], [14] and [15], for example. The numerical treatment of *geometric-type* source terms has by now been thoroughly studied in the community concerned with the numerical solution of the shallow water equations, where such source terms arise from variable bottom topography [16–18]. In some of these developments, the concept of *well-balanced* schemes has been adopted, reflecting the fact that in the absence of time derivatives, the schemes must respect the correct balance between the advective term (the flux) and the source term. These schemes are able to correctly reproduce steady solutions in the presence of source terms. As a way of designing useful schemes for hyperbolic balance laws, the framework of path-conservative numerical schemes, as suggested in [9], is gaining increasing popularity. This is the approach adopted in this paper.

A popular approach to the numerical solution of one-dimensional blood flow in the presence of *geometric* source terms is to write the governing equations in terms of non-conservative variables, such as cross-sectional area A and velocity u, for example. By so doing one can actually express the governing equations in *conservation-law form* and apply standard conservative numerical schemes. However, it is pertinent to point out that such formulations are not *physically conservative* and discontinuous solutions will have the wrong propagation speed. This point is proved theoretically in [19] for the shallow water equations. The same exercise can be carried out for the blood flow equations. Consequently, numerical solutions from this kind of formulations will be incorrect in the presence of elastic jumps. The importance of formulating the mathematical model in terms of conserved variables, that is, cross-sectional area A and volumetric flow rate q, is clearly identified in [10,11]. This issue is further discussed in Müller *et al.* [20], where the importance of a conservative formulation is addressed for the computation of solutions involving elastic jumps or sharp gradients.

The issue of well-balanced schemes for one-dimensional blood flow has already been addressed in the past. Sherwin *et al.* [21], for example, proposed to use a two-rarefaction Riemann solver at locations where material properties vary abruptly and succeeded in devising a well-balanced scheme, although in terms of non-conservative variables. Müller *et al.* [22] use the simplified mathematical model proposed in [10] as a starting point to construct a well-balanced, high-order path-conservative numerical scheme for computing one-dimensional blood flow in both, arteries and veins (collapsible vessels). The proposed numerical scheme in [22] preserves, exactly, steady solutions in any flow regime, that is, sub-, super- and trans-critical. Recently, Delestre and Lagree [23] have also proposed a well-balanced finite-volume scheme for blood flow in the framework of hydrostatic reconstruction [24]. They just considered the case of a single parameter, namely variable reference cross-sectional area.

In this paper, we are concerned with the design of an efficient one-dimensional solver for both arteries and veins, using the formulation based on the conservative variables proposed by Toro and Siviglia [11]. We adopt the framework of path-conservative finite-volume type schemes and extend the Dumbser–Osher–Toro (DOT) Riemann solver [25] for constructing well-balanced fluctuations for a first-order non-oscillatory scheme. Then, we extend the resulting first-order scheme to higher order of accuracy in both space and time by adopting the Arbitrary high-order DERivatives (ADER) methodology [26], with the approach proposed in [27] for solving the associated generalized

Riemann problem (GRP). The full methodology is then extended to deal with realistic networks of vessels, adopting standard techniques for the treatment of boundary conditions and vessel junctions. We validate our numerical scheme through two classes of problems. The first class consists of problems for which exact solutions exist, smooth and discontinuous. Then, we validated both the model and the numerical scheme against results from an *in vitro* model [28] involving a network of compliant vessels, for which both experimental measurements and state-of-the-art numerical solutions have been published.

The rest of the paper proceeds as follows. In section 2, we present the governing equations. In section 3, we briefly review the DOT Riemann solver and propose a modified version that yields a well-balanced fluctuation. Section 4 is devoted to the extension of the first-order scheme to higher order of accuracy in space and time; reported implementations go from first to fifth order of accuracy in space and time; empirically computed convergence rates confirm the expected order of accuracy of the numerical scheme. In section 5, we solve a problem that includes a stationary wave and two RPs chosen to resemble realistic situations, considering both, arteries and veins; we also validate our numerical scheme for a network of elastic vessels for which experimental measurements and numerical solutions are available. Conclusions are drawn in section 6.

2. MATHEMATICAL MODEL

A well established formulation for one-dimensional blood flow is given by the system

$$
\begin{cases}
\partial_t A + \partial_x q = 0, \\
\partial_t q + \partial_x \left(\hat{\alpha} \dfrac{q^2}{A} \right) + \dfrac{A}{\rho} \partial_x p = -f.
\end{cases}
\tag{1}
$$

$A(x,t)$ is the cross-sectional area of the vessel; $q(x,t)$ is the flow rate; $p(x,t)$ is the average internal pressure over a cross section; $f(x,t)$ is the friction force per unit length of the tube; ρ is the fluid density and $\hat{\alpha}$ is a coefficient that depends on the assumed velocity profile. Throughout this work, we will take $\hat{\alpha} = 1$, which corresponds to a blunt velocity profile. For a full description of the model, see [29].

To close the system, we adopt a tube law, whereby the internal pressure $p(x,t)$ is related to the cross-sectional area $A(x,t)$ and other parameters, namely

$$
p(x,t) = p_e(x,t) + \psi(x,t).
\tag{2}
$$

Here $p_e(x,t)$ is the external pressure, prescribed, and $\psi(x,t)$ is the transmural pressure, assumed of the form

$$
\psi(x,t) = \psi(A(x,t), K(x), A_0(x)) = K(x)\phi(A(x,t), A_0(x)).
\tag{3}
$$

$K(x) = K(E(x), h_0(x))$ is a positive function that contains the combined variation in x of $E(x)$, the Young modulus, and of $h_0(x)$, the wall thickness; see [30] for details. The function $\phi(A, x)$ is assumed of the form

$$
\phi(A(x,t), A_0(x)) = \left(\frac{A(x,t)}{A_0(x)} \right)^m - \left(\frac{A(x,t)}{A_0(x)} \right)^n,
\tag{4}
$$

where $A_0(x)$ is the vessel cross-sectional area for a reference configuration, for which the transmural pressure is zero. The parameters m and n are obtained from higher order models or simply computed from experimental measurements. We remark that there are mathematical constraints for the choice of m and n to satisfy hyperbolicity of the equations and for the genuinely non-linear character of the characteristic fields associated with the pressure related eigenvalues; full details are given in [11]. Throughout this work, we assume $m > 0$ and $n \in (-2, 0)$. Typical values for collapsible tubes, such as veins, are $m = 10$, $n = -1.5$; for arteries, $m = 0.5$, $n = 0$. Relations (3) and (4) arise from a mechanical model of the vessel wall displacement under the simplifying assumption of static equilibrium [3].

The spatial variation of the vessel properties K, A_0 and of the external pressure p_e give

$$\partial_x p = \partial_x p_e + K\phi_A \partial_x A + K\phi_{A_0} \partial_x A_0 + \phi \partial_x K, \tag{5}$$

where

$$\phi_A = \frac{\partial \phi}{\partial A}, \quad \phi_{A_0} = \frac{\partial \phi}{\partial A_0}.$$

Substituting (5) into (1) gives

$$\begin{cases} \partial_t A + \partial_x q = 0, \\ \partial_t q + \partial_x \left(\hat{\alpha} \frac{q^2}{A} \right) + \frac{A}{\rho} K\phi_A \partial_x A = -\frac{A}{\rho} \left(\partial_x p_e + K\phi_{A_0} \partial_x A_0 + \phi \partial_x K \right) - f. \end{cases} \tag{6}$$

The right-hand side of the momentum balance equation includes *geometric-type* source terms, which, as stated in Section 1, must be treated carefully.

In this paper, we adopt the reformulation of (6), proposed in [11], namely

$$\partial_t \mathbf{Q} + \mathbf{A}(\mathbf{Q}) \partial_x \mathbf{Q} = \mathbf{S}(\mathbf{Q}), \tag{7}$$

where $\mathbf{Q}$ is given by

$$\mathbf{Q} = \left[A, q, K, A_0, p_e \right]^T, \tag{8}$$

and the coefficient matrix $\mathbf{A}(\mathbf{Q})$ is

$$\mathbf{A}(\mathbf{Q}) = \begin{bmatrix} 0 & 1 & 0 & 0 & 0 \\ c^2 - u^2 & 2u & \frac{A}{\rho}\phi & K\frac{A}{\rho}\phi_{A_0} & \frac{A}{\rho} \\ 0 & 0 & 0 & 0 & 0 \\ 0 & 0 & 0 & 0 & 0 \\ 0 & 0 & 0 & 0 & 0 \end{bmatrix}. \tag{9}$$

Here $u = q/A$ is the cross-sectional averaged velocity of the fluid, $\mathbf{S}(\mathbf{Q})$ is a source term vector

$$\mathbf{S}(\mathbf{Q}) = [0, -f, 0, 0, 0]^T \tag{10}$$

and c is the wave speed

$$c = \sqrt{\frac{A}{\rho} K\phi_A}. \tag{11}$$

System (7) is constructed from (1) by regarding the variable parameters $K(x)$, $A_0(x)$ and $p_e(x,t)$ to be new unknowns, satisfying

$$\partial_t K = 0, \quad \partial_t A_0 = 0, \quad \partial_t p_e = F(x,t), \tag{12}$$

where $F(x,t)$ is a prescribed function for the external pressure. For a thorough mathematical analysis of system (7), see [11]. Here, we recall some of the main features of the system needed for the construction of our numerical scheme. The eigenvalues of (9) are

$$\lambda_1 = u - c, \quad \lambda_2 = \lambda_3 = \lambda_4 = 0, \quad \lambda_5 = u + c. \tag{13}$$

The right eigenvectors of $A(Q)$ corresponding to eigenvalues (13) are

$$
R_1 = \gamma_1 \begin{bmatrix} 1 \\ u-c \\ 0 \\ 0 \\ 0 \end{bmatrix}, \quad
R_2 = \gamma_2 \begin{bmatrix} \frac{A}{\rho}\frac{\phi}{u^2-c^2} \\ 0 \\ 1 \\ 0 \\ 0 \end{bmatrix}, \quad
R_3 = \gamma_3 \begin{bmatrix} \frac{A}{\rho}\frac{K\phi_{A_0}}{u^2-c^2} \\ 0 \\ 0 \\ 1 \\ 0 \end{bmatrix},
$$

$$
R_4 = \gamma_4 \begin{bmatrix} \frac{A}{\rho}\frac{1}{u^2-c^2} \\ 0 \\ 0 \\ 0 \\ 1 \end{bmatrix}, \quad
R_5 = \gamma_5 \begin{bmatrix} 1 \\ u+c \\ 0 \\ 0 \\ 0 \end{bmatrix},
$$

(14)

where γ_i, for $i = 1, ..., 5$, are arbitrary scaling factors.

Under a suitable assumption for coefficients m and n, system (7) is hyperbolic, although not strictly hyperbolic. Hyperbolicity is lost when $|u| = c$, leading to resonance. As noted in [11], there is a possible loss of uniqueness.

The first and fifth characteristic fields are genuinely non-linear and are associated with shocks and rarefactions, whereas the remaining fields are linearly degenerate (LD) and are associated with stationary contact discontinuities. See [11] for conditions on parameters m and n for this to be true. The Riemann invariants associated with the genuinely non-linear fields are

$$
\Gamma_1 = u - \int_{A^*}^{A} \frac{c(\tau)}{\tau}\mathrm{d}\tau, \quad \Gamma_5 = u + \int_{A^*}^{A} \frac{c(\tau)}{\tau}\mathrm{d}\tau,
$$

(15)

where A^* is the cross-sectional area at a reference state. The Riemann invariants associated with the LD fields are given by

$$
\Gamma_1^{LD} = p + \frac{1}{2}\rho u^2, \quad \Gamma_2^{LD} = q.
$$

(16)

In the next section, we describe a scheme to solve (7) numerically.

3. WELL-BALANCED SCHEME FOR ONE-DIMENSIONAL BLOOD FLOW

In this section, we propose a first-order well-balanced numerical scheme. First, we introduce the DOT Riemann solver in its original formulation. Thereafter, the solver is modified to account for specific features of the equations under study.

3.1. Brief review of the DOT solver

The DOT Riemann solver was put forward in [31] as a modified version of the Osher–Solomon Riemann solver [32] for a conservative hyperbolic system. The DOT scheme has also been extended in [25] to deal with non-conservative hyperbolic systems. The DOT solver is inspired by the mathematical theory developed by Dal Maso, LeFloch and Murat [8] and may be seen as a path-conservative scheme, as defined in [9].

A finite-volume type scheme may be constructed by integrating (7) in space and time in the control volume $[x_{i-\frac{1}{2}}, x_{i+\frac{1}{2}}] \times [t^n, t^{n+1}]$, leading to

$$
\begin{aligned}
Q_i^{n+1} = Q_i^n &- \frac{1}{\Delta x}\int_{t^n}^{t^{n+1}}\int_{x_{i-\frac{1}{2}}}^{x_{i+\frac{1}{2}}} A(Q)\partial_x Q\,\mathrm{d}x\mathrm{d}t \\
&- \frac{\Delta t}{\Delta x}\left(D_{i+\frac{1}{2}}^- + D_{i-\frac{1}{2}}^+\right) + \Delta t\,S_i,
\end{aligned}
$$

(17)

where

$$Q_i^n = \frac{1}{\Delta x} \int_{x_{i-\frac{1}{2}}}^{x_{i+\frac{1}{2}}} Q(x, t^n) \, dx, \tag{18}$$

$$S_i = \frac{1}{\Delta t \Delta x} \int_{t^n}^{t^{n+1}} \int_{x_{i-\frac{1}{2}}}^{x_{i+\frac{1}{2}}} S(Q(x,t)) dx dt \tag{19}$$

and

$$D_{i+\frac{1}{2}}^{\pm} = \frac{1}{\Delta t} \int_{t^n}^{t^{n+1}} \mathcal{D}_{i+\frac{1}{2}}^{\pm} \left(Q_{i+\frac{1}{2}}^-(t), Q_{i+\frac{1}{2}}^+(t), \Psi(s) \right) dt. \tag{20}$$

Here, $\Delta x = x_{i+\frac{1}{2}} - x_{i-\frac{1}{2}}$; $\Delta t = t^{n+1} - t^n$; $Q_{i+\frac{1}{2}}^{\pm}(t)$ are limiting data states from left and right arising in the GRP for system (7) at cell interface $x_{i+\frac{1}{2}}$. Details on the GRP will be given in Section 4. Our numerical scheme departs from (17), with suitable approximations for the various integrals.

Given left and right data Q^- and Q^+ for the RP at the cell interface $x_{i+\frac{1}{2}}$, $\mathcal{D}^{\pm}\left(Q^-, Q^+, \Psi(s)\right)$ are defined as fluctuations that depend on a path $\Psi(s)$ and have to satisfy

$$\mathcal{D}^-\left(Q^-, Q^+, \Psi(s)\right) + \mathcal{D}^+\left(Q^-, Q^+, \Psi(s)\right) = \int_0^1 A\left(\Psi\left(Q^-, Q^+, s\right)\right) \frac{\partial \Psi}{\partial s} ds,$$

$$\mathcal{D}^{\pm}\left(Q, Q, \Psi(s)\right) = 0. \tag{21}$$

The path $\Psi = \Psi(Q^-, Q^+, s)$, with $0 \leqslant s \leqslant 1$, is a Lipschitz continuous function that connects the left state Q^- to the right state Q^+ in phase space, satisfying

$$\Psi\left(Q^-, Q^+, 0\right) = Q^-, \quad \Psi\left(Q^-, Q^+, 1\right) = Q^+. \tag{22}$$

The finite-volume type scheme (17) is completely determined once the numerical fluctuations $\mathcal{D}_{i+\frac{1}{2}}^{\pm}$ (analogous to the numerical flux), the numerical source S_i and the space–time integral in (17) are determined. Note that the integral in the first line of (17) vanishes for a first-order method, and the scheme then reads

$$Q_i^{n+1} = Q_i^n - \frac{\Delta t}{\Delta x} \left(\mathcal{D}_{i+\frac{1}{2}}^- + \mathcal{D}_{i-\frac{1}{2}}^+ \right) + \Delta t S_i. \tag{23}$$

In an analogous manner to the determination of the numerical flux in a finite volume scheme, the fluctuations $\mathcal{D}_{i+\frac{1}{2}}^{\pm}$ are found by solving a classical RP (piecewise constant data) for (7) with initial condition

$$Q(x, 0) = \begin{cases} Q_{i+\frac{1}{2}}^- & \text{if } x < x_{i+\frac{1}{2}}, \\ Q_{i+\frac{1}{2}}^+ & \text{if } x > x_{i+\frac{1}{2}}. \end{cases} \tag{24}$$

In particular, for a first-order scheme $Q_{i+\frac{1}{2}}^- = Q_i^n$ and $Q_{i+\frac{1}{2}}^+ = Q_{i+1}^n$. Fluctuations in the DOT scheme, as proposed in [25], are computed as

$$\mathcal{D}_{i+\frac{1}{2}}^{\pm} = \frac{1}{2} \int_0^1 \left[A\left(\Psi\left(Q_{i+\frac{1}{2}}^-, Q_{i+\frac{1}{2}}^+, s \right) \right) \pm \left| A\left(\Psi\left(Q_{i+\frac{1}{2}}^-, Q_{i+\frac{1}{2}}^+, s \right) \right) \right| \right] \frac{\partial \Psi}{\partial s} ds, \tag{25}$$

with the absolute value operator of a matrix defined as

$$|A| = R|\Lambda|R^{-1}, \quad |\Lambda| = \text{diag}\left(|\lambda_1|, |\lambda_2|, ..., |\lambda_N|\right), \tag{26}$$

where $\boldsymbol{R}$ is the matrix of right eigenvectors of $\boldsymbol{A}$ and $\boldsymbol{R}^{-1}$ its inverse. The simplest choice of path $\boldsymbol{\Psi}$ is the *segment*, or *canonical*, path

$$\boldsymbol{\Psi}\left(\boldsymbol{Q}_{i+\frac{1}{2}}^{-}, \boldsymbol{Q}_{i+\frac{1}{2}}^{+}, s\right) = \boldsymbol{Q}_{i+\frac{1}{2}}^{-} + s\left(\boldsymbol{Q}_{i+\frac{1}{2}}^{+} - \boldsymbol{Q}_{i+\frac{1}{2}}^{-}\right). \tag{27}$$

In this case. the final expression for fluctuations (25) reads

$$\mathcal{D}_{i+\frac{1}{2}}^{\pm} = \frac{1}{2}\left\{\sum_{j=1}^{G} \omega_j\left[\boldsymbol{A}\left(\boldsymbol{\Psi}(s_j)\right) \pm |\boldsymbol{A}\left(\boldsymbol{\Psi}(s_j)\right)|\right]\right\}\left(\boldsymbol{Q}_{i+\frac{1}{2}}^{+} - \boldsymbol{Q}_{i+\frac{1}{2}}^{-}\right), \tag{28}$$

after performing numerical integration in (25) using a Gaussian quadrature rule, in which case ω_j and s_j are the j-th weight and Gaussian point coordinate of a quadrature rule with G points. Usually, a Gaussian quadrature rule with 3 points yields satisfactory results, see [17] or [25] for details.

Computational experience in various types of applications have shown that the simple segment path is suitable for obtaining satisfactory numerical solutions. However, for the problems of interest in this paper, early numerical results indicated that a more sophisticated choice of path was necessary.

3.2. Modification of the integration path

Let $\gamma_p(s)$ be a curve in phase space parametrized by a scalar parameter s. We define this curve to be an integral curve of the vector field $\boldsymbol{R}_p$ of system (7), if at each point $\gamma_p(s)$, the tangent vector $\gamma_p'(s)$ to the curve is an eigenvector of $\mathbf{A}(\gamma_p(s))$ in (9) corresponding to the eigenvalue $\lambda_p(\gamma_p(s))$. Furthermore, the expression for the integral curve gives rise to generalized Riemann invariants, which are functions of $\mathbf{Q}$ whose values are invariant along the integral curve $\gamma_p(s)$; see [33] for background. In the case of the LD fields of (9), we have

$$p + \frac{1}{2}\rho u^2 = \bar{\Gamma}_1^{LD} \quad \text{and} \quad q = \bar{\Gamma}_2^{LD}, \tag{29}$$

where $\bar{\Gamma}_{1,2}^{LD}$ are constant values of both, total pressure and volumetric flow rate. Let us also introduce the set Γ_{LD} of all integral curves γ_{LD}, associated to the LD field of (9).

Well-balanced schemes were originally motivated by the need to design numerical approximations to hyperbolic equations with source terms, in such a way as to achieve equilibrium between flux spatial gradient and algebraic source terms, near the steady state. See, for example, [14, 15] and references therein. The precise definition of a well-balanced scheme has evolved, becoming dependent on the particular approach adopted in the design process. The present paper is concerned with a numerical scheme in a class of methods in which the source term is absorbed into an enlarged hyperbolic system with a modified eigenstructure. Then, the definition of a well-balanced scheme becomes quite technical. For the work of this paper, the appropriate definition is that given in [34], which we reproduce later.

Well-balanced numerical scheme: A numerical scheme of the form (23) for system (7) is said to be exactly well-balanced for $\gamma_{LD} \in \Gamma_{LD}$ if, given any steady solution $\mathbf{Q}^{(s)}(x) \in \gamma_{LD}$, $\forall x \in (x_l, x_r) \subset \mathbb{R}$ and initial conditions such that $\boldsymbol{Q}_i^n \in \gamma_{LD}$ $\forall i \in [1, ..., N]$, where N is the number of cells used to discretize the spatial domain (x_l, x_r), then

$$\mathcal{D}_{i+\frac{1}{2}}^{-} + \mathcal{D}_{i-\frac{1}{2}}^{+} = 0, \quad \forall i \in [0, 1, ..., N]. \tag{30}$$

Taking into account that the eigenvalues associated with the stationary contact discontinuity are $\lambda_2 = \lambda_3 = \lambda_4 = 0$ and that the p-th right eigenvector is defined as

$$\boldsymbol{A}\boldsymbol{R}_p = \lambda_p\boldsymbol{R}_p, \tag{31}$$

it follows that a path-conservative numerical scheme (23) with fluctuations (25), will be well balanced if we can guarantee that the path $\boldsymbol{\Psi}(\boldsymbol{Q}_{i+\frac{1}{2}}^{-}, \boldsymbol{Q}_{i+\frac{1}{2}}^{+}, s)$ linking two states $\boldsymbol{Q}_{i+\frac{1}{2}}^{-}$ and $\boldsymbol{Q}_{i+\frac{1}{2}}^{+}$ belonging to an integral curve γ_{LD}, is a parametrization of the arc defined by γ_{LD} [35]. The well-balanced property is also necessary for the correct numerical solution of unsteady problems, as

extensively discussed in [9, 34, 36]. We also show numerical results supporting this fact in this section and in Section 5.

The *segment* path (27), proposed in [25], has been widely used in the numerical solution of several physical problems involving both conservative and non-conservative hyperbolic systems. For the shallow water equations, it guarantees that the resulting numerical scheme is exactly well-balanced for water at rest solutions, see [34]. This is because for the shallow water equations, in fluid at rest conditions, the Riemann invariants associated with the LD field are

$$\Gamma_1^{LD,SWE} = h + b \,, \qquad \Gamma_2^{LD,SWE} = 0 \,, \tag{32}$$

where h is the water depth and b is the bottom elevation. From the relation between h and b in (32), it is evident that the integral curve γ_{LD}^{SWE} in phase-plane (h, b) will be a straight line.

Early numerical experiments on the application of the DOT scheme to system (7) using the segment path (27) showed the inability of the scheme to preserve stationary solutions, that is, solutions for which $u(x, t) = 0$. The reason can be deduced from the analysis of the Riemann invariants associated with the LD characteristic fields. Let us consider a stationary solution defined by states for which the Riemann invariants (16) are

$$p = K \left[\left(\frac{A}{A_0} \right)^m - \left(\frac{A}{A_0} \right)^n \right] + p_e = \bar{\Gamma}_1^{LD} \,, \quad 0 = \bar{\Gamma}_2^{LD} \,. \tag{33}$$

There is a non-linear dependence between K and A. In order to accommodate changes in K, A_0 or p_e, while preserving constancy of the right-hand side in (33), the cross-sectional area A will have to change non-linearly. In other words, the use of the segment path (27) will not preserve steady solutions, not even stationary ones.

Here, we take advantage of the flexible formulation of the DOT Riemann solver, which enables us to numerically integrate along any path. This special characteristic of the DOT solver allows us to define a path that guarantees exact well-balanced properties (up to machine precision) for any steady solution. In this work, we limit ourselves to develop a scheme that only preserves *stationary solutions* exactly, because the main goal of this paper is that of proposing a fast and easy to implement numerical scheme that correctly solves problems where geometric source terms are present. This choice is justified by the following considerations:

- Exact well-balanced schemes for stationary solutions solve unsteady problems in a satisfactory manner as we will see later in this section, and in Section 5, where numerical results are compared with exact solutions and experimental measurements.
- Given the first consideration, we note that ensuring exact well-balancing of any steady solution greatly complicates the implementation of the numerical scheme.

We propose a path that uses the segment path for all variables, except for the cross-sectional area A. The proposed path $\boldsymbol{\Psi}(s)$ reads

$$\boldsymbol{\Psi}(s) = \begin{bmatrix} \bar{A}(s) \\ \bar{q}(s) \\ \bar{K}(s) \\ \bar{A}_0(s) \\ \bar{p}_e(s) \end{bmatrix} = \begin{bmatrix} \bar{\phi}(s)^{-1} \\ q_{i+\frac{1}{2}}^- + s \left(q_{i+\frac{1}{2}}^+ - q_{i+\frac{1}{2}}^- \right) \\ K_{i+\frac{1}{2}}^- + s \left(K_{i+\frac{1}{2}}^+ - K_{i+\frac{1}{2}}^- \right) \\ A_{0,i+\frac{1}{2}}^- + s \left(A_{0,i+\frac{1}{2}}^+ - A_{0,i+\frac{1}{2}}^- \right) \\ p_{e,i+\frac{1}{2}}^- + s \left(p_{e,i+\frac{1}{2}}^+ - p_{e,i+\frac{1}{2}}^- \right) \end{bmatrix} . \tag{34}$$

$\bar{\phi}(s)$ is a path for relation (4), defined as

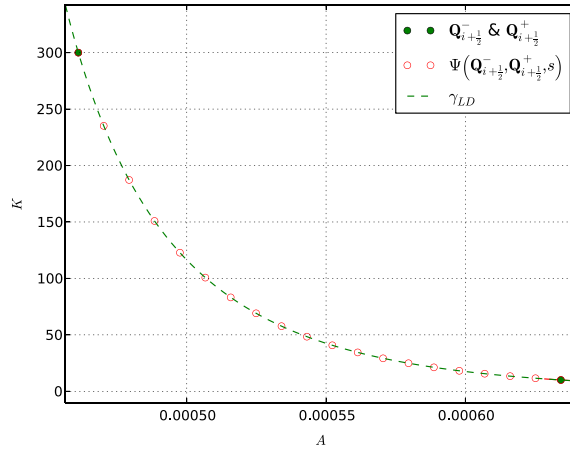$$\bar{\phi}(s) = \frac{\bar{\Gamma}(s) - \bar{p}_e(s)}{\bar{K}(s)} \,, \tag{35}$$

Figure 1. Integration path $\mathbf{\Psi}(s)$ (34), on the (A, K) phase-plane, and integral curve γ_{LD} associated with the LD field for the case of fluid at rest.

where $\bar{\Gamma}(s)$ is

$$\bar{\Gamma}(s) = \bar{\Gamma}^{1,-}_{LD,i+\frac{1}{2}} + s\left(\bar{\Gamma}^{1,+}_{LD,i+\frac{1}{2}} - \bar{\Gamma}^{1,-}_{LD,i+\frac{1}{2}}\right). \tag{36}$$

Once that $\bar{\phi}(s)$ is known, we compute $\bar{A}(s)$ from (4) using a globally convergent Newton method for $n \neq 0$. It is possible to verify that a solution always exits for $A > 0$ and is unique. When $n = 0$ the solution is explicit.

Parametrizations (35) and (36) are designed to guarantee that the numerical scheme will preserve stationary solutions exactly. In fact, in the case of fluid at rest, $\bar{\Gamma}(s)$ will be a constant because

$$\bar{\Gamma}^{1,+}_{LD,i+\frac{1}{2}} = \bar{\Gamma}^{1,-}_{LD,i+\frac{1}{2}},$$

and the resulting path will be a parametrization of the integral curve γ_{LD}.

Figure 1 shows the proposed path $\mathbf{\Psi}(s)$, on the (A, K) phase-plane, together with the integral curve γ_{LD} corresponding to the Riemann invariant associated to the LD field for a *fluid at rest* solution. Use of the segment path would correspond to compute integral (25) in phase space along a straight line, and this would clearly result in a non-well-balanced solution, as we shall see later in this section and in Section 5.

The fluctuation for the DOT solver using the proposed path is

$$\mathcal{D}^{\pm}_{i+\frac{1}{2}} = \frac{1}{2}\left(\sum_{j=1}^{G} \omega_j \left\{ \left(A\left(\mathbf{\Psi}(s_j)\right) \pm \left|A\left(\mathbf{\Psi}(s_j)\right)\right|\right) \left.\frac{\partial \mathbf{\Psi}}{\partial s}\right|_{s_j} \right\}\right). \tag{37}$$

Note that, because of our choice of path, vector $\frac{\partial \mathbf{\Psi}}{\partial s}$ cannot be taken out of the integral (25), as performed when using the segment path. Derivatives for most variables are easily computed, besides that for $\bar{A}(s)$, which might be an implicit function of ϕ, so that its derivative at each quadrature point $s = s_j$ is computed as

$$\frac{\partial \bar{A}}{\partial s}(s_j) = \left(\frac{\partial \bar{\phi}}{\partial s}(s_j) - \left.\frac{\partial \phi}{\partial \bar{A}_0}\right|_{s=s_j} \frac{\partial \bar{A}_0}{\partial s}(s_j)\right)\left(\left.\frac{\partial \phi}{\partial \bar{A}}\right|_{s=s_j}\right)^{-1}. \tag{38}$$

The numerical scheme (23) with fluctuations (37) and path (34) is a first-order well-balanced numerical scheme for system (7). In the next section, we illustrate the performance of the proposed scheme for some test problems.

Table I. Parameters used for Riemann problems 1 to 3: domain length L; reference stiffness K_{ref}; tube law exponential coefficients m and n; reference cross-sectional area $A_{0,ref}$; relative location of the initial discontinuity x_g/L and output time t_{end}.

Test	L [m]	K_{ref} [Pa]	m	n	$A_{0,ref}$ [m^2]	x_g/L	t_{end} [s]
1	0.2	58725.0	1/2	0	3.1353×10^{-4}	0.5	0.1
2	0.2	58725.0	1/2	0	3.1353×10^{-4}	0.3	0.007
3	0.2	5.0	10	-3/2	1.0000×10^{-4}	0.3	0.025

Table II. State variables for Riemann problems 1 to 3. α represents the non-dimensional cross-sectional area with respect to the reference area $A_{0,T} = \alpha_{0,T} A_{0,ref}$, with $T = L, R$. External pressure values are given in millimeter of mercury. α^* is a value obtained from solving (2) for A^*, imposing $p^* = 80.0 \, mmHg$.

Test	α_L	$\alpha_{0,L}$	u_L	K_L	$p_{e,L}$	α_R	$\alpha_{0,R}$	u_R	K_R	$p_{e,R}$
1	α_L^*	2.0	0.0	K_{ref}	75.0	α_R^*	1.0	0.0	$10.0\,K_{ref}$	85.0
2	1.6	0.5	1.	K_{ref}	30.0	1.05	1.0	0.0	$10.0\,K_{ref}$	0.0
3	0.9	1.1	0.0	K_{ref}	10.0	1.6	1.3	0.0	$10.0\,K_{ref}$	5.0

3.3. Numerical results for the DOT solver

We solve RPs

$$\begin{rcases} \partial_t \boldsymbol{Q} + \boldsymbol{A}(\boldsymbol{Q})\partial_x \boldsymbol{Q} = \boldsymbol{0}, \quad x \in \mathcal{R}, \quad t > 0, \\ \boldsymbol{Q}(x,0) = \begin{cases} \boldsymbol{Q}_L & \text{if } x < x_g, \\ \boldsymbol{Q}_R & \text{if } x > x_g \end{cases} \end{rcases} \tag{39}$$

for the homogeneous version of (7). As already said, RPs are the building blocks of our numerical scheme and, in general, of a broad class of finite-volume type schemes. If an exact solution to such a problem is available, it constitutes a useful tool to validate numerical schemes, because solutions to this kind of problems tend to challenge the numerical scheme to solve the variety of wave patterns given by the underlying PDEs. In this section, RPs are solved exactly using an implementation of the exact solution to problem (39) put forward in [11].

The following RPs were designed using parameters reported in applications regarding cardiovascular mathematics. Besides the first RP, whose solution is stationary, the remaining RPs are idealized time-dependent tests for real-world related situations and should be considered as a tool for checking the accuracy and robustness of the proposed numerical scheme for ranges of parameters found in the human body. Mechanical properties and geometrical characteristics for each RP are given in Table I, whereas initial conditions are specified in Table II. Chosen values resemble mechanical properties and geometric characteristics in the thoracic aorta (RP1 and RP2 with parameters taken from [1]) and in the internal jugular vein (IJV; RP3 with parameters based on [37] and [38]). For all tests the spatial domain was discretized with 100 cells and a Courant number of $CFL = 0.9$ was used.

RP1 is designed to test the well-balanced properties of the DOT scheme. We set $p^*(x,0) = 80.0 \, mmHg$ as initial condition and assign the corresponding cross-sectional area using (2). The problem presents variations in vessel wall stiffness K, cross-sectional area at reference state A_0 and external pressure p_e. Moreover, we have that $\alpha_L^* < 1.0$ and $\alpha_R^* > 1.0$. The exact solution of this problem is identically the initial condition, and the numerical scheme will have to preserve this initial condition. Figure 2, top frame, shows numerical results from the DOT solver using the proposed path (34). The bottom frame shows corresponding results obtained using the segment path (27). Our scheme preserves the initial condition, whereas the results obtained with the non-well-balanced scheme are erroneous, very far from the exact stationary solution.

In the case of RP2, we have set up the (idealized) problem of a systolic pressure and flow peak arriving to a certain region of the thoracic aorta. In order to challenge our numerical scheme, we have also chosen to compress the left side of the aorta, that is, the part that was already reached by the
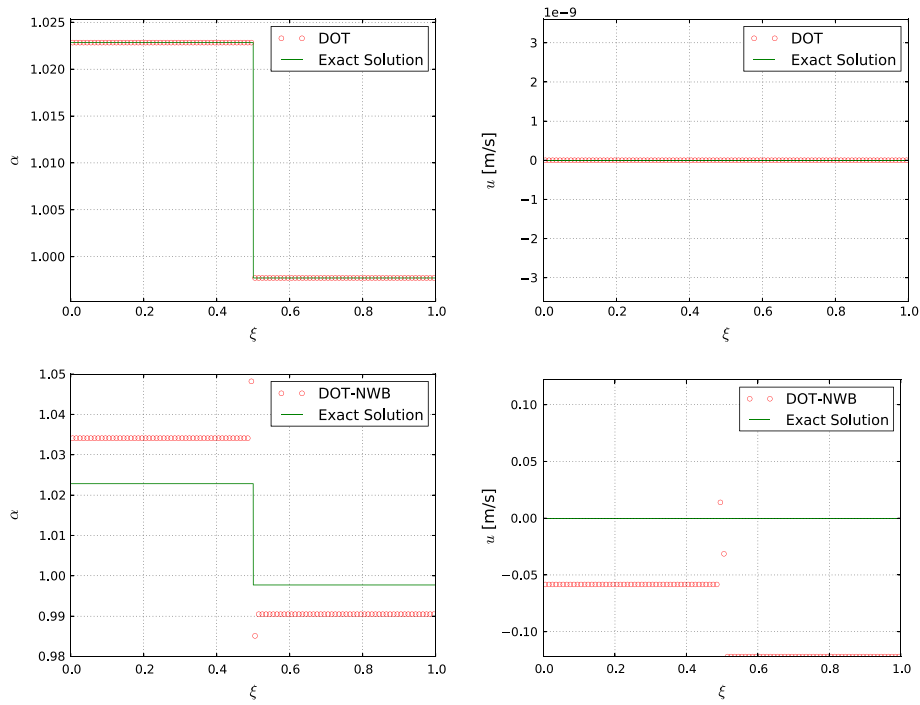
Figure 2. Results for RP1 obtained using the first-order Dumbser–Osher–Toro (DOT) solver with well-balanced fluctuation (37) (top) and the first-order DOT solver with non-well-balanced fluctuation (28) (bottom). Shown results are for non-dimensional cross-sectional area (left) and velocity (right) versus non-dimensional length. Note different ranges for velocity plots.

systolic peak. Moreover, we have set the portion of the aorta to the right of the initial discontinuity to be 10 times stiffer than the portion to the left. The wave pattern of such an idealized situation will result in a partial reflection of the incoming wave front. Numerical results are shown in Figure 3. Although results for the well-balanced DOT solver, top frame, compare well with the exact solution, the DOT solver using the segment path, bottom frame, is unable to correctly capture the states to the left and right of the stationary contact discontinuity. This example shows that the inability of the non-well-balanced scheme to solve stationary problems will also influence its suitability to solve unsteady problems.

In RP3, we represent the case of an IJV during a Valsalva maneuver, in which the subject exhales while closing all airways. This maneuver produces a high central venous pressure, reaching values of around 40 mmHg, see [39]. In this idealized problem setup, we consider the case for which the valve present at the proximal end, relative to the heart, of the IJV suddenly fails to fulfil its function of preventing venous reflux toward the head. We have chosen to set a negative pressure as initial condition in the distal portion of the IJV, which would correspond to the situation verified in a standing subject. Finally, the proximal end of the IJV was set to be 10 times stiffer than the distal one. The exact solution, as well as numerical results for this problem, are shown in Figure 4. We observe that a strong elastic jump develops and travels toward the head, whereas a rarefaction travels in the direction of the heart. Also in this case, we achieve a good agreement between the exact solution and the numerical results for the well-balanced DOT solver. To conclude, it is worth noting that for this case the non-well-balanced scheme performs better than for the previous tests. This behaviour can be easily understood by having a look at Figure 5. In this figure, we show states across the stationary contact discontinuity, the integral curve γ_{LD} (continuous line) and the segment path (dashed line) in the non-dimensional $(\alpha, \hat{K})$ phase-plane for RP2 and RP3. We define non-dimensional quantities as

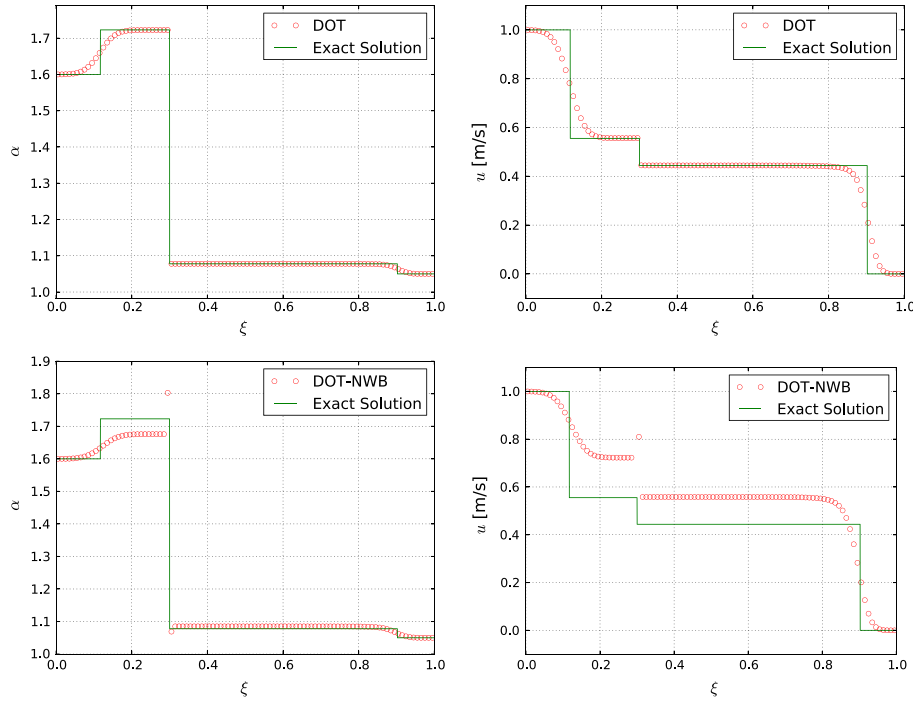$$\alpha = \frac{A}{A^*} \quad \hat{K} = \frac{K}{K^*},$$

Figure 3. Exact solution and numerical results for RP2 regarding an (idealized) systolic pressure and peak flow arriving to a portion of the thoracic aorta with discontinuous mechanical properties and external compression. Results obtained using the first-order Dumbser–Osher–Toro (DOT) solver with well-balanced fluctuation (37) (top) and the first-order DOT solver with non-well-balanced fluctuation (28) (bottom). Shown results are for non-dimensional cross-sectional area (left) and velocity (right) versus non-dimensional length.

with $A^* = \min(A_{0,L}, A_{0,R})$ and $K^* = \min(K_L, K_R)$. The jump in α is smaller for RP3 in comparison with that for RP2. Therefore, using the segment path for RP3, implies small deviations from the integral curve γ_{LD}. Take for example, $\hat{K} = 4$. Using the segment path for RP2 implies an error in the evaluation of α of approximately $\Delta\alpha_{RP2} = \alpha_{LD} - \alpha_{seg} = 0.17$, whereas in the case of RP3, we have $\Delta\alpha_{RP3} = \alpha_{LD} - \alpha_{seg} = 0.002$. The bigger deviation from the integral curve γ_{LD} by the segment path in RP2 is further penalizing the performance of the non-well-balanced scheme by the fact that for this RP the wall stiffness K is fourth order of magnitude bigger than for RP3. In the hypothetical case of two RPs where the jump in α across the stationary contact discontinuity is equal for both tests, the value of K will be the key factor for the amplification/reduction of errors underwent by using an incorrect path.

The results shown so far are for a first-order scheme. In the next section, we extend the proposed methodology to higher order of accuracy in both space and time.

4. HIGH-ORDER EXTENSION

In order to extend our first-order well-balanced scheme to high order of accuracy in space and time, we adopt the fully discrete ADER framework [26]. ADER-type schemes require three main steps:

- Nonlinear spatial reconstruction
- Solution of the GRP at cell interfaces to compute fluctuations (or numerical fluxes).
- In the presence of source terms, accurate space–time integration of source terms is also needed to compute the numerical source.

For path-conservative ADER schemes, one also needs to accurately compute the double integral on the first line in (17).
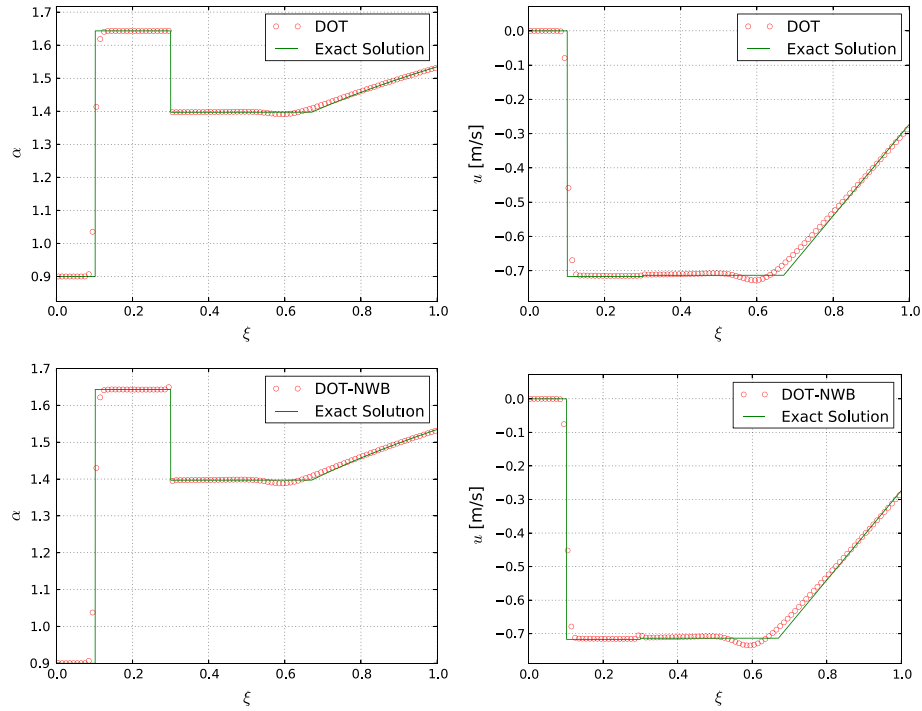
Figure 4. Exact solution and numerical results for RP3, regarding an (idealized) Valsava maneuver effect on an internal jugular vein with incompetent valve and discontinuous mechanical properties. Results obtained using the first-order Dumbser–Osher–Toro (DOT) solver with well-balanced fluctuation (37) (top) and the first-order DOT solver with non-well-balanced fluctuation (28) (bottom). We show results for non-dimensional cross-sectional area (left) and velocity (right) versus non-dimensional length.
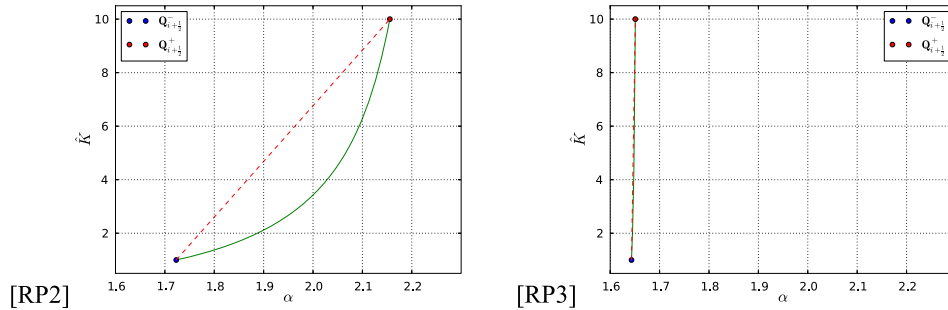

Figure 5. States across the stationary contact discontinuity, integral curve γ_{LD} (continuous line) and segment path (dashed line) in non-dimensional $(\alpha, \hat{K})$ phase-plane for RP2 and RP3.

For each of these steps there are several possibilities. In the case of the spatial reconstruction, one could use any standard essentially non-oscillatory or weighted essentially non-oscillatory (WENO) reconstruction [40, 41]. Regarding the solution of the GRP, we refer the reader to [42] for a thorough review on four methods so far available. In this paper, we adopt the GRP solver proposed by Dumbser, Enaux and Toro [27], the DET solver. This has the advantage of avoiding the Cauchy–Kowalewski procedure and can deal with stiff source terms. This scheme has been applied successfully to severe tests problems that include vessel collapse, which result in stiffness [20].

4.1. The ADER scheme

We proceed with a brief explanation of the steps followed for the implementation of the ADER scheme with the Dumbser–Enaux–Toro (DET) GRP solver. For a more detailed description, see [25, 27, 43] and the above cited references.

4.1.1. Spatial reconstruction.
For the spatial reconstruction, we use the WENO methodology [41], by which, for time level t^n, we reconstruct element-wise polynomials of the type

$$\boldsymbol{w}_h = \boldsymbol{w}_h(x, t^n) = \sum_{l=1}^{M+1} \psi_l(x) \hat{\boldsymbol{w}}_l \,, \tag{40}$$

where M is the polynomial degree of the spatial reconstruction, $\psi_l(x)$ are the corresponding basis functions and $\hat{\boldsymbol{w}}_l$ are the expansion coefficients. The expansion coefficients are computed by applying a reconstruction operator on cell averages $\boldsymbol{Q}_j^n$, over a defined stencil $\mathcal{S}_i$ (for details, see [44]).

4.1.2. The DET solver.
Once the spatial reconstruction is available, we proceed with the solution of the GRP at cell interface $x = x_{i+\frac{1}{2}}$ (locally at $x = 0$)

$$\left. \begin{array}{l} \partial_t \boldsymbol{Q} + \boldsymbol{A}(\boldsymbol{Q})\partial_x \boldsymbol{Q} = \boldsymbol{0}, \quad x \in \mathcal{R}, \quad t > 0, \\[2mm] \boldsymbol{Q}(x, 0) = \left\{ \begin{array}{ll} \boldsymbol{P}_i(x) & \text{if } x < 0, \\ \boldsymbol{P}_{i+1}(x) & \text{if } x > 0. \end{array} \right. \end{array} \right\}, \tag{41}$$

where $\boldsymbol{P}_i(x)$ and $\boldsymbol{P}_{i+1}(x)$ are non-linear reconstructions of the data to the left and right of the cell interface. The solution of the GRP will yield a time-dependent solution at the interface, locally along $x/t = 0$, and will be used to evaluate integrals in (20) to compute the fluctuations. We remark that the notation $x/t = 0$ to describe the interface means $x = 0$ and $t > 0$; when $t = 0$, one refers to the initial conditions of the problem, and the solution of the PDE is strictly given for $t > 0$.

A feature of the DET solver is the time evolution of the initial data left and right of the interface. To this end, a space–time local discontinuous-Galerking (DG) scheme is used, which will provide a local space–time polynomial $\boldsymbol{Q}_h = \boldsymbol{Q}_h(x, t)$ to be later used in (20), as well as in (19). We start by transforming system (7) to a reference space–time element $T_E = [0; 1] \times [0; 1]$ with normal coordinates ξ and τ, related to the physical domain by $x = x_{i-\frac{1}{2}} + \Delta x\, \xi$ and $t = t^n + \Delta t\, \tau$. The resulting system reads

$$\partial_\tau \boldsymbol{Q}_h + \boldsymbol{A}^* \partial_\xi \boldsymbol{Q}_h = \boldsymbol{S}^*, \tag{42}$$

with modified Jacobian and source term vector

$$\boldsymbol{A}^* := \frac{\Delta t}{\Delta x} \boldsymbol{A}(\boldsymbol{Q}_h), \quad \boldsymbol{S}^* := \Delta t\, \boldsymbol{S}(\boldsymbol{Q}_h)\,.$$

In order to simplify the notation, we introduce the following operators:

$$[a, b]^\tau = \int_0^1 a(\xi, \tau)\, b(\xi, \tau)\, \mathrm{d}\xi, \quad <a, b>_{T_E} = \int_0^1 \int_0^1 a(\xi, \tau)\, b(\xi, \tau)\, \mathrm{d}\xi \mathrm{d}\tau. \tag{43}$$

Next, we multiply (42) by a space–time basis function $\theta = \theta(\xi, \tau)$ and integrate over the reference element T_E. Using integration by parts for the time derivative term, we obtain

$$[\theta, \boldsymbol{Q}_h]^1 - <\partial_t \theta, \boldsymbol{Q}_h>_{T_E} + <\theta, \boldsymbol{A}^* \partial_\xi \boldsymbol{Q}_h>_{T_E} = [\theta, \boldsymbol{w}_h]^0 + <\theta, \boldsymbol{S}^*>_{T_E}. \tag{44}$$

We use the same space–time basis functions θ, for $\boldsymbol{Q}_h$ and $\boldsymbol{A}^* \partial_\xi \boldsymbol{Q}_h$, so that

$$\boldsymbol{Q}_h(\xi, \tau) = \sum_{l=1}^{(M+1)^2} \theta_l \hat{\boldsymbol{Q}}_l, \quad \boldsymbol{A}^* \partial_\xi \boldsymbol{Q}_h(\xi, \tau) = \sum_{l=1}^{(M+1)^2} \theta_l \widehat{\boldsymbol{A}^* \partial_\xi \boldsymbol{Q}}_l. \tag{45}$$

We obtain expansion coefficients $\hat{\boldsymbol{Q}}_l$ by a fixed-point iteration procedure, see [27] for details, in which at each iteration step, we solve the following system:

$$\left([\theta_k, \theta_l]^1 - <\partial_t \theta_k, \theta_l>_{T_E}\right) \hat{\boldsymbol{Q}}_l^{m+1} - <\theta_k, \theta_l>_{T_E} \boldsymbol{S}^*\left(\hat{\boldsymbol{Q}}_l^{m+1}\right) = [\theta, \boldsymbol{w}_h]^0 - <\theta_k, \theta_l>_{T_E} \boldsymbol{A}^* \widehat{\partial_\xi \boldsymbol{Q}}_l^m .$$

(46)

The solution to the GRP at time τ is found by solving a classical RP using the space–time reconstructed states extrapolated to both sides of the cell interface, see [42]. The source term space–time average (19) and the non-conservative product space–time average present in (17) are computed by numerical integration using $\boldsymbol{Q}_h$ and a quadrature rule of appropriate accuracy. We adopt a nodal basis function given by Gauss–Lobatto quadrature points and the corresponding Lagrange polynomials intersecting these points for both polynomials, $\boldsymbol{w}_h$ and $\boldsymbol{Q}_h$ [43]. This choice reduces the computational cost for the solution of the GRP and for the evaluation of integrals present in (17), because states to be used at each quadrature point are already known.

Remarks 1
A couple of remarks on some practical aspects of the scheme are in order.

- *Well-balanced WENO reconstruction.* In order to preserve well-balanced properties of the numerical scheme, care is required in applying the WENO reconstruction operator. In fact, if we have a stationary solution $\boldsymbol{Q}^s$ with all states belonging to the integral curve γ_{LD} associated with the Riemann invariant of the LD field, then the output states $\boldsymbol{w}_h(x)$ of the WENO reconstruction operator must lie in the same integral curve γ_{LD}. We recall that in the case of a stationary solution, the associated Riemann invariant, besides the trivial condition $q^s(x,t) = 0$, is given by relation (33). Therefore, the reconstruction operator has to be applied to the internal pressure p instead of A, in order to preserve exact well-balanced solutions for the stationary case. This procedure is based on the same principle as that proposed in [45] for the shallow water equations.

- *Non-conservative products in the local DG data evolution procedure.* The term $\boldsymbol{A}^* \partial_\xi \boldsymbol{Q}_h$ present in (44) must be computed exactly in the case of a stationary solution. Normally, this term is obtained by first computing the expansion coefficients of spatial derivatives of $\boldsymbol{Q}_h$ using the following weak identity

$$< \theta_k, \theta_l > \widehat{\partial_\xi \boldsymbol{Q}}_l = < \theta_k, \partial_\xi \theta_l > \hat{\boldsymbol{Q}}_l ,$$

(47)

and then proceeding to a matrix vector product to obtain

$$\boldsymbol{A}^* \widehat{\partial_\xi \boldsymbol{Q}}_l = \boldsymbol{A}^* \widehat{\partial_\xi \boldsymbol{Q}}_l .$$

(48)

Equation (48) involves the use of $\widehat{\partial_\xi A}_l$, which again will not be exactly computed because $A^s(x)$ for a stationary solution will not necessarily be a polynomial. To overcome this problem, we explicitly compute the second component of $\boldsymbol{A}^* \widehat{\partial_\xi \boldsymbol{Q}}_l$ so that

$$\boldsymbol{A}^* \widehat{\partial_\xi \boldsymbol{Q}}_l = \begin{bmatrix} \widehat{\partial_\xi q}_l \\ \frac{\hat{q}_l}{\hat{A}_l} \widehat{\partial_\xi q}_l + \hat{A}_l \widehat{\partial_\xi \beta}_l \\ 0 \\ 0 \\ 0 \end{bmatrix} .$$

(49)

In this case, as for the spatial reconstruction, we keep tract of an auxiliary variable $\beta_h(\xi, \tau) = \theta_l \hat{\beta}_l$ during the local data evolution procedure. β is given by

$$\beta = \frac{1}{2}\left(\frac{q}{A}\right)^2 + \frac{p}{\rho} .$$

(50)

Because for a stationary solution β is constant, it is computed exactly for any order of accuracy of our numerical scheme.

Table III. Convergence results for the ADER scheme. N is the number of cells. Errors are computed for variable A. CPU times are reported for all tests.

Scheme	N	L^1	L^2	L^∞	$\mathcal{O}(L^1)$	$\mathcal{O}(L^2)$	$\mathcal{O}(L^\infty)$	t_{CPU} [s]
ADER-O2	4	1.07e-05	1.23e-05	2.55e-05	—	—	—	0.02
	8	2.49e-06	2.94e-06	7.64e-06	2.1	2.1	1.7	0.04
	16	5.69e-07	6.99e-07	2.02e-06	2.1	2.1	1.9	0.13
	32	1.34e-07	1.69e-07	5.13e-07	2.1	2.0	2.0	0.39
ADER-O3	4	4.20e-06	4.74e-06	8.50e-06	—	—	—	0.05
	8	5.64e-07	6.90e-07	1.46e-06	2.9	2.8	2.5	0.12
	16	7.17e-08	8.96e-08	1.97e-07	3.0	2.9	2.9	0.33
	32	8.99e-09	1.13e-08	2.51e-08	3.0	3.0	3.0	0.99
ADER-O4	4	1.02e-06	1.15e-06	1.69e-06	—	—	—	0.14
	8	1.40e-07	2.05e-07	5.73e-07	2.9	2.5	1.6	0.25
	16	1.17e-08	1.58e-08	4.44e-08	3.6	3.7	3.7	0.74
	32	8.22e-10	1.06e-09	2.97e-09	3.8	3.9	3.9	2.30
ADER-O5	4	1.78e-06	2.00e-06	3.40e-06	—	—	—	0.22
	8	6.92e-08	8.42e-08	1.71e-07	4.7	4.6	4.3	0.54
	16	2.28e-09	2.84e-09	6.17e-09	4.9	4.9	4.8	1.60
	32	7.57e-11	9.59e-11	2.41e-10	4.9	4.9	4.7	5.00

4.2. Empirical convergence rate study

Here, we carry out a convergence rate study in order to verify that the expected theoretical order of accuracy of the proposed numerical scheme is actually attained. To this end, we construct a test problem for a modified non-linear system of equations that is a perturbation of the original system via a source term vector. In this manner, we obtain a smooth, exact solution of a non-homogeneous non-linear system. Note that for this procedure to work, the numerical scheme must be able to compute solutions to non-homogeneous systems to the high order of accuracy. We proceed to prescribe a smooth function $\hat{Q}(x,t)$ that will be the exact solution of the perturbed system. Here, we choose

$$
\hat{Q}(x,t) = \begin{bmatrix} \hat{A}(x,t) \\ \hat{q}(x,t) \\ \hat{K}(x) \\ \hat{A}_0 \\ \hat{p}_e(x) \end{bmatrix} = \begin{bmatrix} \tilde{A} + \tilde{a}\,\sin\left(\frac{2\pi}{L}x\right)\cos\left(\frac{2\pi}{T_0}t\right) \\ \tilde{q} - \tilde{a}\,\frac{L}{T_0}\cos\left(\frac{2\pi}{L}x\right)\sin\left(\frac{2\pi}{T_0}t\right) \\ \tilde{K} + \tilde{k}\,\sin\left(\frac{2\pi}{L}x\right) \\ \tilde{A}_0 + \tilde{a}_0\,\sin\left(\frac{2\pi}{L}x\right) \\ \tilde{P}_e + \tilde{p}_e\,\sin\left(\frac{2\pi}{L}x\right) \end{bmatrix}. \tag{51}
$$

Inserting (51) into (7), we obtain the following inhomogeneous system

$$
\partial_t \mathbf{Q} + \mathbf{A}(\mathbf{Q})\partial_x \mathbf{Q} = \hat{\mathbf{S}}(x,t). \tag{52}
$$

The resulting source term $\hat{\mathbf{S}}(x,t)$ reflects the fact that (51) is not a solution of the original system (7). $\hat{\mathbf{S}}(x,t)$ can be computed exactly using algebraic manipulators; its expression is not reproduced here. For the convergence rate study the following parameters were used: $L = 1.0\,m$, $T_0 = 1.0\,s$, $\tilde{A} = 4.0 \times 10^{-4}\,m^2$, $\tilde{a} = 4.0 \times 10^{-5}\,m^2$, $\tilde{q} = 0.0\,m^3\,s^{-1}$, $\tilde{K} = 50.0\,KPa$, $\tilde{k} = 500.0\,Pa$, $\tilde{P}_e = 0.0\,Pa$, $\tilde{p}_e = 50.0\,Pa$, $m = 1/2$ and $n = 0$.

Table III displays the empirical convergence rates for the proposed numerical scheme up to fifth order of accuracy in space and time. Errors were measured in the norms L_1, L_2 and L_∞. The expected convergence rates are reached for all norms.

Remark on high accuracy. High accuracy means computational efficiency. Obviously, for a fixed mesh a low-order scheme will generally be faster than its higher order extension. But this is not the way to evaluate the efficiency of numerical schemes. Instead, given an error dimmed to be
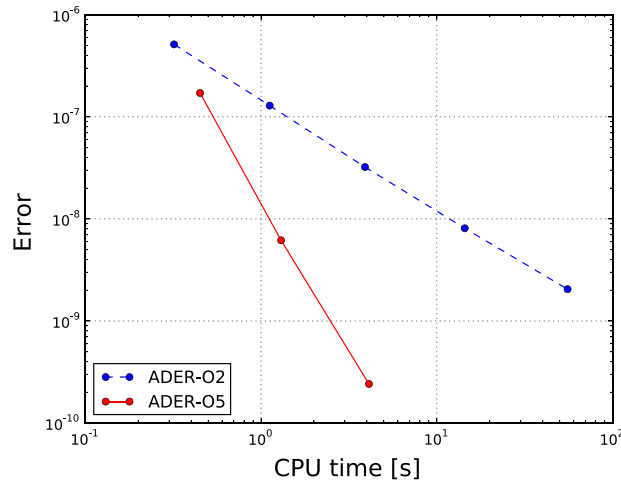
Figure 6. Error versus CPU time for second- and fifth-order implementations of the ADER scheme.

acceptable, the question is which method will attain that error at the lowest computational cost. Figure 6 shows error versus CPU time for the second- and fifth-order implementations of the ADER schemes presented in this paper. The CPU time is that resulting from a sequence of successively refined meshes. It is seen that, for example, given an acceptable error of $E = 10^{-9}$, the fifth-order ADER method will be almost two orders of magnitude more efficient than the second-order ADER method. The first-order method, not shown, will appear as an almost horizontal line, suggesting that achieving the prescribed error of $E = 10^{-9}$ will be almost an impossible task in practice. The implication of the efficiency point just made is that for constructing a global, close model for the human circulation system, the high accuracy of the numerical method to be employed is of paramount importance. See also considerations made in Section 5.3.

After the description of the high-order extension of the proposed numerical scheme and the empirical convergence rate study, we proceed to validate its robustness and efficiency through a series of tests.

4.3. Tests with exact solutions containing discontinuities

Here, we show numerical solutions to RPs 1 to 3, described in Section 3.3. Figure 7 displays results obtained from the third-order ADER scheme of this paper. The high-order scheme preserves all the good features of the first-order DOT scheme, such as well-balanced properties and correct solutions for the two unsteady RPs 2 and 3. In addition, note that for RPs containing discontinuous solutions, there is an improvement of the resolution of both, elastic jumps and rarefactions, as compared with the first-order results shown in Figures 3 and 4.

5. VALIDATION FOR FLOW IN NETWORKS OF ELASTIC BLOOD VESSELS

In this section, we implement a computational model to simulate flow in an *in vitro* model of the human arterial system. The *in vitro* model was presented in [28] and was further studied in [46]. The model consists of 37 rubber tubes resembling major arteries, a pump to simulate the heart and terminal resistances fulfilling the role of the peripheral circulation. For details on the topography of the network, description of mechanical properties, geometry of the vessels, terminal resistances and flow rate measured at the root of the ascending aorta, see [28] and [46]. The experimental setup in [28] and the carefully reported details of all necessary parameters allow the reader to implement the computational representation of the *in vitro* model. This makes possible a thorough validation of any given solver intended for one-dimensional blood flow simulations.
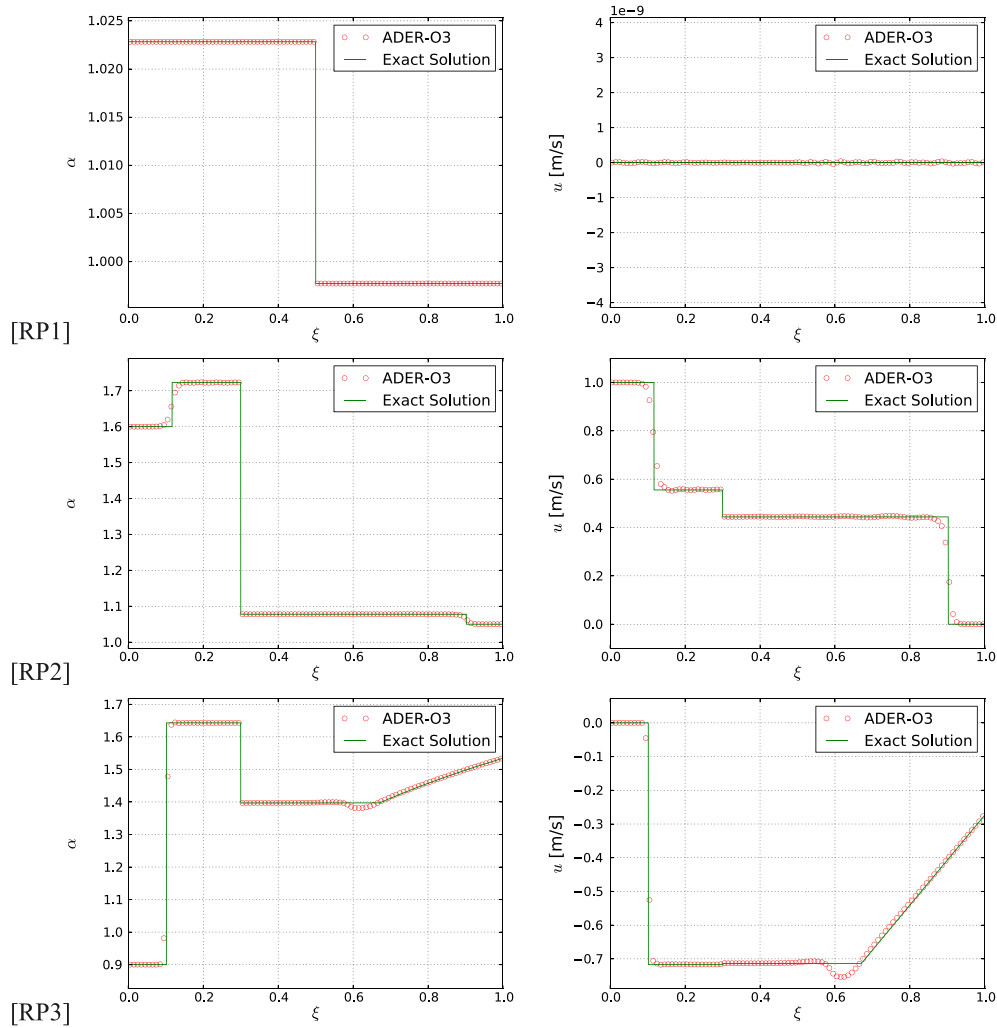
Figure 7. Results for Riemann problems 1 to 3 using the third-order average displaced emissions rate (ADER) scheme with well-balanced fluctuation (37). Shown results are for non-dimensional cross-sectional area (left) and velocity (right) versus non-dimensional length.

Application of the numerical scheme just proposed to the modelling of networks requires the treatment of specific boundary conditions and algorithms for treating vessel junctions. We must prescribe flow rate at the proximal end of the ascending aorta and terminal resistances at distal ends of the network. Flow rate and terminal resistances were treated as in [47]. For junctions, the methodology proposed in [48] was chosen.

The *in vitro* model has variations of reference cross-sectional area A_0 in most vessels, so that this test problem is perfectly suited to validate three aspects of the proposed methodology, namely (i) well-balanced properties of the numerical scheme and their relevance in the context of one-dimensional blood flow; (ii) ability to reproduce experimental measurements; and (iii) accuracy and efficiency of the resulting solver.

We adopted the same spatial discretization used in [46]: vessels longer than 1.5 cm were divided in non-overlapping cells of a maximum length of 2 cm; for vessels shorter than 1.5 cm a single cell was used. Computations were performed using a $CFL = 0.9$, which results in an average time step of approximately $\Delta t = 7.7 \times 10^{-4}\, s$. We note that the time step Δt is computed at each time step, in order to advance as much as possible in time during each step, within the linear stability limit of unity of our explicit scheme. Experimental measurements for pressure and flow rate and numerical results reported in [46] were made available to us by Dr. Jordi Alastruey.
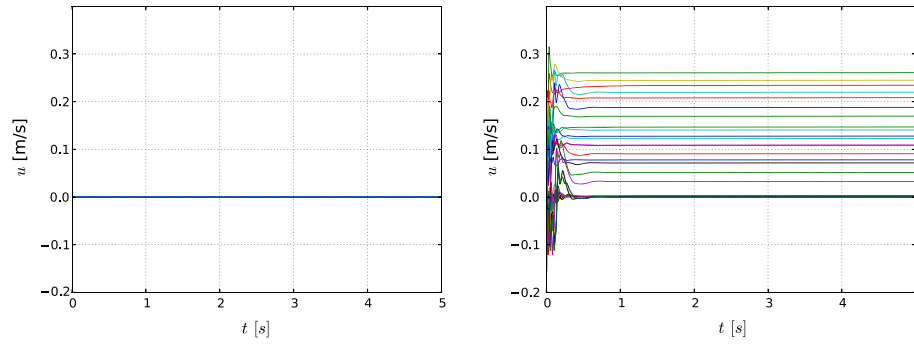
Figure 8. Computed velocities at midpoint location versus time for all 37 vessels of the *in vitro* model for dead man test. Left frame shows results obtained using a weighted essentially non-oscillatory (WENO) reconstruction in terms of pressure p and volumetric flow rate q; right frame shows results obtained using a WENO reconstruction for cross-sectional area A and q.

5.1. Assessing the influence of a correct WENO spatial reconstruction

For this section, we devised a *trivial* test, called here the *dead man test*, which at first glance, might seem irrelevant, as blood flow in arteries is never stationary. We prescribe zero pressure and no flow as initial conditions and assign transparent boundary conditions at all distal ends of the network. The exact solution to this problem is identically the initial condition. Solving this problem with a numerical scheme that naively treats the source terms will cause the code to crash. One reason for this is that supercritical flow will develop and the methodology used for dealing with junctions will not support this kind of flow regime. In Figure 8, we show velocities at midpoint location versus time for all vessels of the network. The results on the left frame were obtained with a third-order implementation of the ADER scheme with a WENO reconstruction in terms of pressure p and volumetric flow rate q. The right frame of Figure 8 shows the numerical solution obtained with a WENO reconstruction for cross-sectional area A and q. This example motivates a point already mentioned earlier. Even though the fluctuations and the local DG data evolution procedure are well balanced, performing the WENO reconstruction of the wrong set of variables will produce spurious oscillations in the numerical solution.

Next we apply the non-well-balanced version of the ADER scheme that produces the wrong results of Figure 8 to the unsteady problem reported in [28]. Figure 9 shows that this scheme will compute erroneous results, as in the case of the trivial dead man test. The consequences of such an approach observed in the case of a stationary test also affect the unsteady solution. In fact, flow rates at some locations are biased by the non-well-balanced nature of the numerical scheme. In cases for which no reference solution is available, this kind of error can lead to totally erroneous results.

5.2. Numerical versus experimental results

In Figure 10 we compare experimental measurements, numerical results reported in [46] and our numerical results for a third-order implementation of the ADER scheme. Results are for pressure and flow rate at different locations of the network. Our numerical results compare very well with both experiments and published state-of-the-art numerical results.

We observe larger amplitudes of high-frequency oscillations in the reference numerical results, compared with our approximation, especially for flow rates in the left renal and right carotid arteries. This behaviour can be explained by the following observations. The spatial discretization used in [46] implies using only one or two computational cells for some vessels. Contrary to the reference results that where obtained using a DG numerical scheme that evolves spatial polynomials in time, we use a finite-volume type scheme. The higher the order of our finite-volume type scheme, the larger will be the stencil to be used in the non-linear WENO reconstruction. In many cases, the WENO stencil will involve cells that are outside of the computational domain. In such cases, we use ghost cells, whose state values are given by prescribed boundary condition data. This procedure is
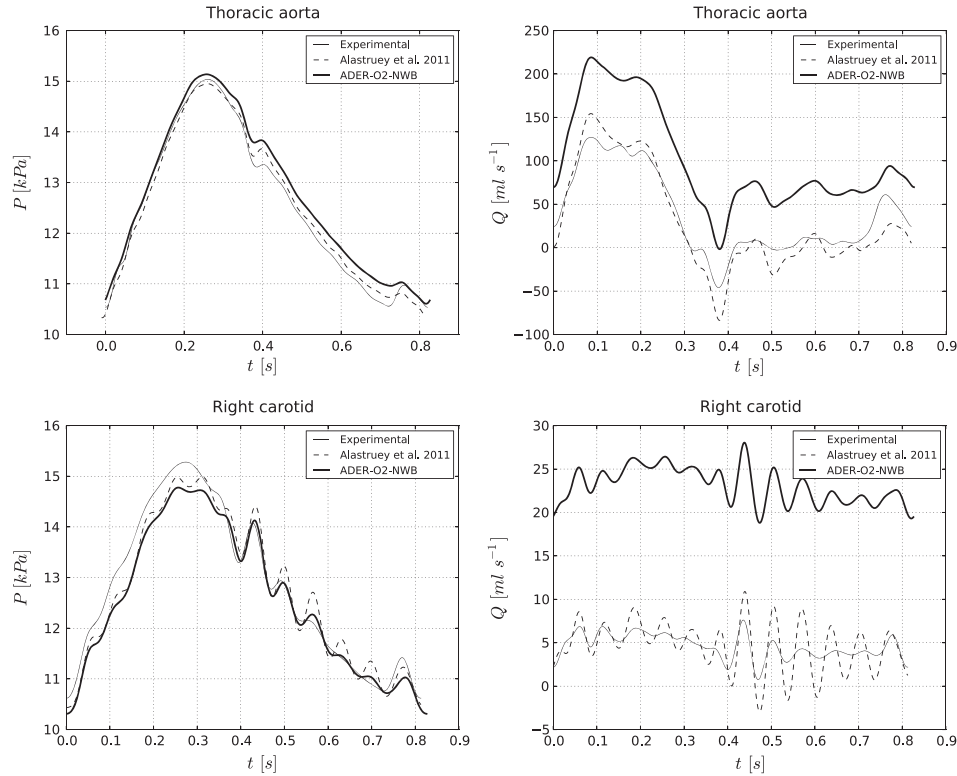
Figure 9. Performance of non-well-balanced scheme for an unsteady problem.

not strictly equivalent to the treatment of boundary conditions operated for the DG scheme in [46]. Moreover, we note that the non-linear spatial reconstruction will eventually damp some oscillations. This might seem an apparent drawback of our finite-volume type scheme. In reality, it is the WENO spatial reconstruction operator that allows us to solve problems with discontinuous or very sharp gradients, as shown in Section 4.

Finally, it is worth noting that the amplitude of the high-frequency oscillations is overestimated by the purely elastic model used for the vessel walls and does not reflect the actual amplitudes registered in the experimental measurements. Alastruey *et al.* [46] have shown that using a viscoelastic vessel wall model provides a better numerical approximation of experimental measurements. Future work will regard the incorporation of such tube law models in our solver.

5.3. Computational cost and efficiency

The computational cost for one cardiac cycle of the test presented in the previous section is reported in Table IV. CPU times include the treatment of junctions and the prescription of boundary conditions. The time step was defined at each time level by imposing a $CFL = 0.9$, with an average value of $\Delta t = 7.71 \times 10^{-4}\, s$, for the spatial discretization proposed in [46]; the code was run on a workstation with an Intel Core i7-2600 processor with 4 cores (3.40 GHz clock speed) and 8 GB of RAM. Considering that the code for the network solver was not optimized, these results allow us to claim that our numerical scheme is computationally cheap. The main features of the numerical method are its low computational cost, the fact of being well-balanced and its robustness, even for its higher order implementations, that allows us to solve problems with large vessel deformations, as in the case of veins.

In Figure 11, we show a comparison of numerical results for the first-order scheme presented in Section 3 and for the high-order implementations up to fourth order. The first-order results were obtained on a series of refined meshes (Table IV), whereas high-order solutions refer to the mesh
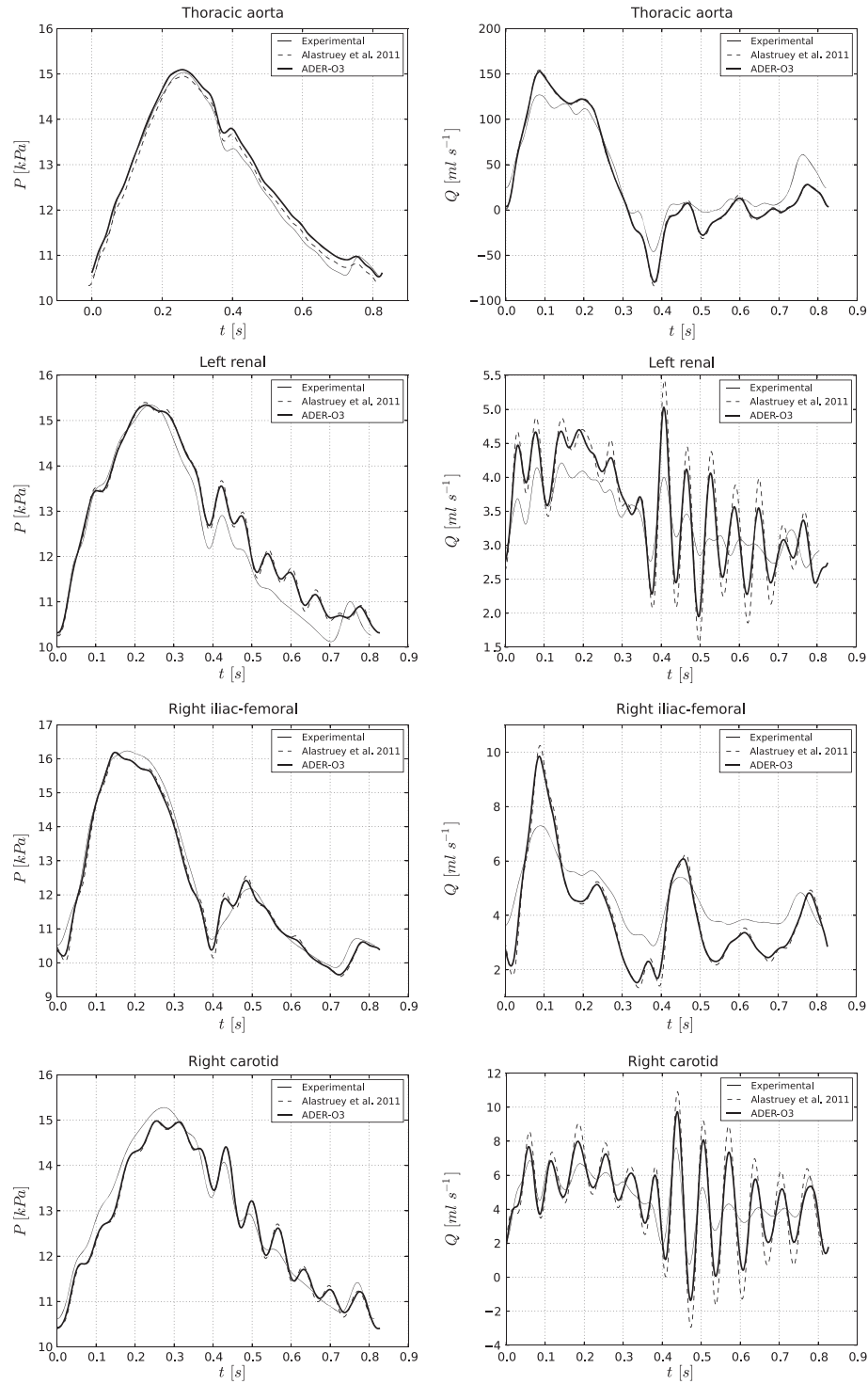
Figure 10. Comparison of our numerical results in third-order mode against experimental measurements and numerical results by Alastruey *et al.* [46].

Table IV. Computational cost for runs presented in this paper. nDOF is number of degrees of freedom of the space–time polynomial $\boldsymbol{Q}_h = \boldsymbol{Q}_h(\xi, \tau) = \hat{\boldsymbol{Q}}_l \theta_l$, computed during the local predictor step and later used to solve the GRP.

Tests	nDOF	Δx [cm]	t_{cpu} [s]
DOT-O1	—	2	3.11
DOT-O1-REF1	—	1	17.78
DOT-O1-REF2	—	0.5	53.82
DOT-O1-REF3	—	0.25	151.31
ADER-O2	1124	2	4.60
ADER-O3	2529	2	8.99
ADER-O4	4496	2	21.37

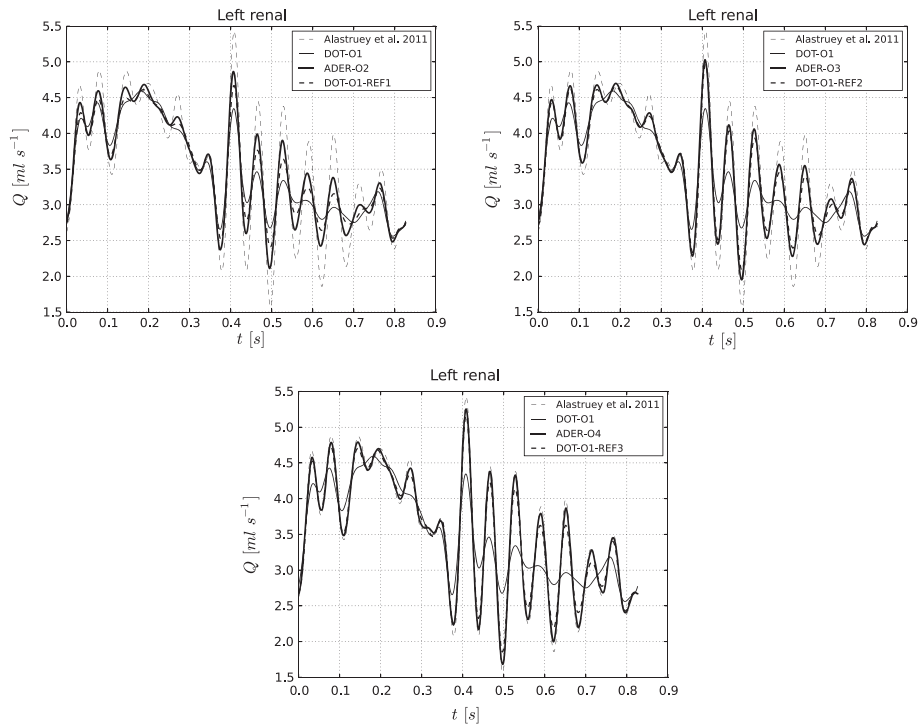GRP, generalized Riemann problem; DOT, Dumbser–Osher–Toro; ADER, Arbitrary high-order DERivatives.

Figure 11. Comparison of numerical results obtained with the first-order scheme on refined grids and with the higher order implementations on the original grid. Higher order schemes deliver a more accurate solution with less computational time, see Table IV.

used in [46]. As expected, doubling the number of cells at each refinement step yields a numerical solution similar to the corresponding high-order approximation. Nevertheless, the high-order solutions are always slightly more accurate and computationally cheaper than the first-order solutions, see Table IV. These observations confirm our considerations made in Section 4 with respect to the efficiency of high-order schemes.

6. CONCLUDING REMARKS

We have constructed a well-balanced high-order numerical scheme for one-dimensional flow in blood vessels with variable mechanical and geometrical properties. Having adopted a suitable, recently proposed mathematical model, we have devised a modified version of the DOT Riemann

solver for non-conservative systems, so that the associated first-order monotone scheme preserves stationary solutions exactly. We have then extended the first-order DOT-based scheme to higher order of accuracy in space and time following the ADER approach. An empirical convergence rate study confirms that the expected theoretical order of accuracy is effectively achieved by the numerical scheme. Theoretically, the ADER approach allows arbitrary order of accuracy in space and time. Through a series of carefully chosen test problems, we have verified the well-balanced property of the numerical scheme, as well as its ability to solve problems including elastic jumps and large gradients, for which exact solutions are available. The proposed numerical scheme is then applied to a network of elastic vessels for which experimental measurements and state-of-the-art numerical solutions are available. The performance of our scheme turns out to be very satisfactory.

In current and future work, the adopted mathematical model and proposed numerical scheme will be extended to include more general tube laws with the aim of constructing a closed global model for the human circulation system involving arteries, veins, capillaries and cerebro-spinal fluid.

REFERENCES

1. Alastruey J, Parker KH, Peiró J, Byrd SM, Sherwin SJ. Modelling the circle of Willis to assess the effects of anatomical variations and occlusions on cerebral flows. *Journal of Biomechanics* 2007; **40**:1794–1805.
2. Liang FY, Fukasaku K, Liu H, Takagi S. A computational model study of the influence of the anatomy of the circle of Willis on cerebral hyperperfusion following carotid artery surgery. *Biomedical Engineering Online* 2011; **10**:84.
3. Formaggia L, Lamponi D, Quarteroni A. One-dimensional models for blood flow in arteries. *Journal of Engineering Mathematics* 2003; **47**:251–276.
4. Casulli V, Dumbser M, Toro EF. Semi-implicit numerical modeling of axially symmetric flows in compliant arterial systems. *International Journal for Numerical Methods in Biomedical Engineering* 2012; **28**:257–272.
5. Blanco PJ, Pivello MR, Urquiza SA, Feijóo RA. On the potentialities of 3D-1D coupled models in hemodynamics simulations. *Journal of Biomechanics* 2009; **42**:919–930.
6. Dumas L, Boutouyrie P, Bozec E. An optimal reconstruction of the human arterial tree from doppler echotracking measurements. *Genetic and Evolutionary Computation Conference*, Philadelphia, PA, 2012.
7. Canic S. Blood flow through compliant vessels after endovascular repair: wall deformations induced by the discontinuous wall properties. *Computing and Visualization in Science* 2002; **4**:147–155.
8. Dal Maso G, LeFloch PG, Murat F. Definition and weak stability of nonconservative products. *Journal de Mathématiques Pures et Appliquées* 1995; **74**:483–548.
9. Parés C. Numerical methods for nonconservative hyperbolic systems: a theoretical framework. *SIAM Journal on Numerical Analysis* 2006; **44**:300–321.
10. Toro EF, Siviglia A. Simplified blood flow model with discontinuous vessel properties: analysis and exact solutions. In *Modelling Physiological Flows Series: Modelling, Simulation and Applications*, Ambrosi D, Quarteroni A, Rozza G (eds). Springer-Verlag: Milan Dordrecht Heidelberg London New York, 2012.
11. Toro EF, Siviglia A. Flow in collapsible tubes with discontinuous mechanical properties: mathematical model and exact solutions. *Communications in Computational Physics* 2013; **13**(2):361–385.
12. Roe P. Upwind differencing schemes for hyperbolic conservation laws with source terms. In *Nonlinear Hyperbolic Problems*, Carasso C, Serre D, Raviart P-A (eds). Springer: Berlin Heidelberg, 1987; 41–51.
13. Bermudez A, Vázquez-Cedón ME. Upwind methods for hyperbolic conservation laws with source terms. *Computers & Fluids* 1994; **23**(8):1049–1071.
14. LeVeque RJ. Balancing source terms and flux gradients in high-resolution Godunov methods: the quasi-steady wave-propagation algorithm. *Journal of Computational Physics* 1998; **146**:346–365.
15. Vázquez-Cedón ME. Improved treatment of source termns in upwind schemes for the shallow water equations in channels with irregular geometry. *Journal of Computational Physics* 1999; **148**:497–526.
16. Bernetti R, Titarev VA, Toro EF. Exact solution of the Riemann problem for shallow water equations with discontinuous bottom geometry. *Journal of Computational Physics* 2008; **227**:3212–3243.
17. Canestrelli A, Siviglia A, Dumbser M, Toro EF. Well-balanced high-order centred schemes for non-conservative hyperbolic systems. Applications to shallow water equations with fixed and mobile bed. *Advances in Water Resources* 2009; **32**:834–844.
18. Castro CE, Toro EF, Käser M. ADER scheme on unstructured meshes for shallow water: simulation of tsunami waves. *Geophysical Journal International* 2012; **189**:1505–1520.

19. Toro EF. *Shock-Capturing Methods for Free-Surface Shallow Flows*. Wiley and Sons Ltd.: Chichester, 2001.
20. Müller LO, Montecinos GI, Toro EF. Some issues in modelling venous haemodynamics. In *Numerical Methods for Hyperbolic Equations: Theory and Applications. An international conference to honour Professor E. F. Toro*, Vázquez-Cendón ME, Hidalgo A, García-Navarro P, Cea L (eds). CRC Press, Taylor & Francis Group: Boca Raton London New York Leiden, 2013; 347–354.
21. Sherwin SJ, Formaggia L, Peiró J, Franke V. Computational modelling of 1D blood flow with variable mechanical properties and its application to the simulation of wave propagation in the human arterial system. *International Journal for Numerical Methods in Fluids* 2003; **43**:673–700.
22. Müller LO, Parés C, Toro EF. Well-balanced high-order numerical schemes for one-dimensional blood flow in vessels with varying mechanical properties. *Journal of Computational Physics* 2013; **242**:53–85.
23. Delestre O, Lagree PY. A well-balanced finite volume scheme for blood flow simulation. *International Journal for Numerical Methods in Fluids* 2012; **72**:177–205. DOI: 10.1002/fld.3736.
24. Audusse E, Bouchut F, Bristeau M, Klein R, Perthame B. A fast and stable well-balanced scheme with hydrostatic reconstruction for shallow water flows. *SIAM Journal on Scientific Computing* 2004; **25**:2050–2065.
25. Dumbser M, Toro EF. A simple extension of the Osher Riemann solver to non-conservative hyperbolic systems. *Journal of Scientific Computing* 2011; **48**:70–88.
26. Toro EF, Millington R, Nejad L. Towards very high order Godunov schemes. In *Godunov Methods. Theory and Applications*, Toro EF (ed.). Kluwer/Plenum Academic Publishers: New York, 2001.
27. Dumbser M, Enaux C, Toro EF. Finite volume schemes of very high order of accuracy for stiff hyperbolic balance laws. *Journal of Computational Physics* 2008; **227**:3971–4001.
28. Matthys KS, Alastruey J, Peiró J, Khir AW, Segers P, Verdonck PR, Parker KH, Sherwin SJ. Pulse wave propagation in a model human arterial network: assessment of 1-D numerical simulations against in vitro measurements. *Journal of Biomechanics* 2007; **40**:3476–3486.
29. Formaggia L, Quarteroni A, Veneziani A. *Cardiovascular Mathematics: Modeling and Simulation of the Circulatory System*. Springer-Verlag: Milan, 2009.
30. Brook BS, Falle SAEG, Pedley TJ. Numerical solutions for unsteady gravity-driven flows in collapsible tubes: evolution and roll-wave instability of a steady state. *Journal of Fluid Mechanics* 1999; **396**:223–256.
31. Dumbser M, Toro EF. On Universal Osher-type schemes for general nonlinear hyperbolic conservation laws. *Communications in Computational Physics* 2011; **10**:635–671.
32. Osher S, Solomon F. Upwind difference schemes for hyperbolic systems of conservation laws. *Mathematics of Computation* 1982; **38**:339–374.
33. LeVeque RJ. *Finite-Volume Methods for Hyperbolic Problems*. Cambridge University Press: Cambridge, 2004.
34. Parés C, Castro M. On the well-balance property of Roe's method for nonconservative hyperbolic systems. Applications to shallow-water systems. *ESAIM: Mathematical Modelling and Numerical Analysis* 2004; **38**:821–852.
35. Munoz-Ruiz ML, Parés C. On the convergence and well-balanced property of path-conservative numerical schemes for systems of balance laws. *Journal of Scientific Computing* 2011; **48**:274–295.
36. Castro MJ, LeFloch PG, Munoz-Ruiz ML, Parés C. Why many theories of shock waves are necessary: convergence error in formally path-consistent schemes. *Journal of Computational Physics* 2008; **227**:8107–8129.
37. Attinger EO. Wall properties of veins. *IEEE Transactions on Bio-Medical Engineering* 1969; **16**:253–261.
38. Pedley TJ, Brook BS, Seymour RS. Blood pressure and flow rate in the giraffe jugular vein. *Philosophical Transactions: Biological Sciences* 1996; **351**:855–866.
39. Gisolf J, van Lieshout JJ, van Heusden K, Pott F, Stok WJ, Karemaker JM. Human cerebral venous outflow pathway depends on posture and central venous pressure. *Journal of Physiology* 2004; **560**:317–327.
40. Harten A, Engquist B, Osher S, Chakravarthy S. Uniformly high order accurate essentially non-oscillatory schemes, III. *Journal of Computational Physics* 1987; **71**:231–303.
41. Jiang G, Shu C. Efficient implementation of weighted ENO schemes. *Journal of Computational Physics* 1996; **126**:202–228.
42. Montecinos GI, Castro CE, Dumbser M, Toro EF. Comparison of solvers for the generalized Riemann problem for hyperbolic systems with source terms. *Journal of Computational Physics* 2012; **231**:6472–6494.
43. Hidalgo A, Dumbser M. ADER Schemes for nonlinear systems of stiff advection-diffusion-reaction equations. *Journal of Scientific Computing* 2011; **48**:173–189.
44. Dumbser M, Balsara DS, Toro EF, Munz C. A unified framework for the construction of one-step finite volume and discontinuous Galerkin schemes on unstructured meshes. *Journal of Computational Physics* 2008; **227**:8209–8253.
45. Dumbser M, Castro M, Parés C, Toro EF. ADER schemes on unstructured meshes for nonconservative hyperbolic systems: applications to geophysical flows. *Computers & Fluids* 2009; **38**:1731–1748.
46. Alastruey J, Khir AW, Matthys KS, Segers P, Sherwin SJ. Pulse wave propagation in a model human arterial network: assessment of 1-D visco-elastic simulations against in vitro measurements. *Journal of Biomechanics* 2011; **44**:2250–2258.
47. Alastruey J, Parker KH, Peiró J, Sherwin SJ. Lumped parameter outflow models for 1-d blood flow simulations: effect on pulse waves and parameter estimation. *Communications in Computational Physics* 2008; **4**:317–336.
48. Sherwin SJ, Franke V, Peiró J, Parker KH. One-dimensional modelling of a vascular network in space-time variables. *Journal of Engineering Mathematics* 2003; **47**:217–250.